

Synthesis of Amorphous and Crystalline Hollow Manganese Oxide Nanotubes with Highly Porous Walls Using Carbon Nanotube Templates and Enhanced Catalytic Activity

Trung-Dung Dang,[†] Arghya Narayan Banerjee,^{*,‡} Sang Woo Joo,^{*,‡} and Bong-Ki Min[§]

[†]School of Chemical Engineering, Hanoi University of Science and Technology, first DaiCoViet, Hanoi, Vietnam

[‡]School of Mechanical Engineering and [§]Center for Research Facilities, Yeungnam University, Gyeongsan 712-749, South Korea

S Supporting Information

ABSTRACT: A novel rapid fabrication method was developed for the first time to prepare hollow manganese oxide nanotubes with porous walls, using sacrificial carbon nanotube templates. Multiwalled carbon nanotubes (CNTs) are coated with amorphous manganese oxide layers by acidic reduction of potassium permanganate solution. The rapid synthesis process with the evolution of gaseous byproduct yields very high porosity in the coated manganese oxide layers. Subsequent heat treatment leads to the removal of CNT templates, resulting in the formation of amorphous and crystalline hollow manganese oxide nanotubes with highly porous walls. The porous hollow nanotubes were found to provide excellent catalytic performances in the degradation of organic dye at ambient conditions by virtue of the very high surface reaction sites within the porous hollow tubular structures. These novel nanostructures of hollow nanotubes with porous walls are promising for a series of applications such as hydrogen storage, sensing, supercapacitance, and catalysis, among others.

1. INTRODUCTION

One-dimensional (1D) inorganic nanomaterials have provided tremendous opportunities for many highly important applications, including molecular detectors, nanoelectromechanical (NEMS) systems, energy-harvesting materials, sensors, nano-electronics, optoelectronics, nanobiotechnology, and nanofluidics.^{1–3} Among these 1D nanostructures, hollow nanotubes have recently gained additional interest because of their large active surface areas, leading to novel applications in drug delivery, energy storage, detection of neural signals, magnetism, and sensors.^{4–6} In general, methods for the fabrication of inorganic hollow 1D nanomaterials can be divided into two categories. One is no-template processes, including Ostwald ripening, galvanic replacement, self-rolling, and the Kirkendall effect.^{4,7–12} The other uses templates, such as sacrificial 1D nanostructures and porous matrixes that are subsequently removed.^{13–18} Between these two categories, template-assisted methods are particularly interesting because architectural nanostructures with tuned properties can be fabricated by these methods with some novel applications.⁵ In this respect, metal oxide hollow nanotubes are particularly important because the compositions and properties of these oxides can be extended to a wide spectrum of binary, ternary, and tertiary compounds; semimetal, semiconductor, and insulating nanomaterials; and magnetic, electrical, and superconducting nanostructures.⁴

In particular, manganese oxides are technologically important materials with a variety of applications, such as catalytic materials, ion sieves, rechargeable batteries, chemical sensing devices, magnetic devices, field-emission devices, hydrogen-storage media, and microelectronics.^{19–24} Micro-, meso-, and nanoporous manganese oxides, as well as layered claylike manganese oxide nanomaterials, can be prepared by a variety of

routes. Many reports are available in the literature regarding synthetic processes that include either oxidation of Mn(II) in basic solution;²⁵ oxidation by MnO_4^- ,²⁶ O_2 , $\text{K}_2\text{S}_2\text{O}_8$, and H_2O_2 ;²⁷ or reduction of MnO_4^- using different routes.²⁸ The reduction of KMnO_4 in dilute aqueous H_2SO_4 produces manganese oxide nanoparticles with a hexagonal layer structure.²⁹ Regarding the synthesis of 1D manganese oxide nanomaterials, nanowires of $\alpha\text{-MnO}_2$ are synthesized using coordination polymers,^{30–32} whereas single-crystalline $\beta\text{-MnO}_2$ nanorods are prepared by hydrothermal or electrochemical methods.^{20,21,33,34}

Manganese oxides with novel morphologies or nanostructures can lead to new avenues for their application. Manganese oxide-coated carbon nanotubes (CNTs) or other organic/inorganic nanofibers or MnO_2 nanotube–CNT or –graphene nanocomposites are thus prepared by a variety of methods, including chemical in situ coating, electrodeposition, and hydrothermal syntheses for high-performance energy-storage devices,^{20–22,33} lithium batteries, rechargeable zinc–air batteries, electrocatalytic water splitting systems, and supercapacitor applications.^{33–38} To the best of our knowledge, however, no report on the synthesis of hollow manganese oxide nanotubes with highly porous walls has been published so far. A recent work on the application of MnO_2 nanorods as efficient hydrogen-storage media has opened up new opportunities for cost-effective hydrogen-storage materials in clean-energy applications.²² The reason for the better hydrogen-storage capability of this kind of nanostructure is the improved specific

Received: February 19, 2014

Revised: April 26, 2014

Accepted: May 15, 2014

Published: May 15, 2014

surface area, which can store a large amount of hydrogen in a relatively small volume and thus can easily be transported. Hollow nanotubes offer much higher specific surface areas than solid nanorods and are thus expected to be very useful for economically viable hydrogen reservoir systems. The catalytic degradation of toxic organic molecules with MnO_2 nanostructures can also be improved by using hollow MnO_2 nanotubes with porous walls by virtue of the increased active surface area, providing better catalytic activity for wastewater treatment.^{39,40}

In this study, a novel, yet simple and cost-effective, method is developed for the first time to prepare hollow manganese oxide nanotubes (MONTs), with highly porous walls, using multi-walled carbon nanotubes (MWCNTs) as templates. An acidic permanganate reaction is performed to coat manganese oxide onto the MWCNTs, followed by heat treatments to obtain hollow nanotubes. The method has the advantage of producing a uniform coating of amorphous MnO_2 with a homogeneous morphology on the surface of MWCNTs. The thickness of the coating can be tuned by controlling the manganese ion concentration in the precursor solution. Upon heat treatment of the as-coated MWCNTs in ambient atmosphere, hollow amorphous MnO_2 nanotubes (a:MONTs) are formed through the removal of CNT templates, which are further converted into hollow crystalline Mn_2O_3 nanotubes (c:MONTs) at higher temperatures. Most importantly, the novelty of these nanostructures is that the walls of the hollow nanotubes (both a:MONTs and c:MONTs) are highly porous. Moreover, the porosity, wall thickness, and lateral and radial dimensions of these hollow nanotubes can be efficiently controlled by controlling the initial template dimensions, as well as Mn-to-C molar ratio in the precursor solution. Previously, hollow nanotubes of metal oxides such as ZnO , WO_3 , TiO_2 , and also MnO_2 with solid walls have been reported,^{13,16,21,41} but this is the first report on the formation of hollow oxide nanotubes with highly porous walls, which offer significantly enhanced specific surface areas and, thus, are extremely useful in interfacial and surface-related applications such as high-efficiency energy storage, sensing, and catalysis, among others. Indeed, this novel nanostructure, for example, exhibits a great improvement in the catalytic degradation of rhodamine B (RhB) solution (presented here) for environmental remediation. Additionally, as the method is very simple and cost-effective, it opens up new possibilities for diverse device applications of similar types of hollow nanostructures.

2. EXPERIMENTAL SECTION

2.1. Preparation of Hollow Nanotubes. The fabrication of hollow a:MONTs and c:MONTs was achieved by a three-step process. In the first step, MWCNTs (Sigma-Aldrich, Seoul, South Korea) were functionalized by oxidization in a mixture of H_2SO_4 and HNO_3 (1:1 volume ratio) for 5 min with sonication. The oxidized CNTs were then washed five times with deionized (DI) water and centrifuged at 5000 rpm for 10 min. In the second step, amorphous MnO_2 was coated onto the as-functionalized MWCNTs by the reaction of KMnO_4 (Sigma-Aldrich, Seoul, South Korea) and HCl (Sigma-Aldrich, Seoul, South Korea) at room temperature. This step actually started with mixing of 0.001 mol of KMnO_4 , 20 mL of DI water, and functionalized CNTs with a magnetic stirrer (Fisher Scientific, Seoul, South Korea), followed by sonication for 15 min and stirring for 30 min. Then, 2 mL of 6 M HCl was added to this mixture dropwise. After the mixture had been stirred at room

temperature for 4 h, MnO_2 -coated CNTs formed, which were then separated, washed five times with DI water, and dried in air at room temperature for 48 h. To monitor the effect of the Mn ion concentration on the uniformity and thickness of the coating layers on the CNTs, the molar ratio of KMnO_4 to CNT was varied roughly from 0.2 to 0.5 by changing the amount of MWCNTs in the precursor solution. In the third step, hollow manganese oxide nanotubes (a:MONT, c:MONT) were formed by heat treatments of the coated samples (at different temperatures) to remove the CNT templates. The annealing was done in a furnace (Fisher Scientific, Seoul, South Korea) under ambient atmosphere at different temperatures of 400, 600, and 900 °C to observe the variations in the morphology and phase of the nanomaterials. To prepare control samples for comparison, MnO_2 nanopowder was synthesized by the reaction of 10 mL of 0.1 M KMnO_4 and 2 mL of 6 M HCl with stirring at room temperature for 4 h. The powder was then heated according to the same heating processes as described above.

2.2. Characterization. For a systematic comparison, the control samples, manganese oxide-coated CNT samples before heat treatment, and heat-treated hollow a:MONT/c:MONT samples were characterized by X-ray powder diffraction (XRD) using a PANalytical X'Pert PRO X-ray diffractometer with $\text{Cu K}\alpha$ radiation (40 kV, 30 mA) and a PIXcell solid-state detector. The patterns were recorded at room temperature with a step size of 0.02°. The surface morphologies, nanostructures, and compositions of the as-synthesized samples were recorded by field-emission scanning electron microscopy (FESEM, Hitachi S-4200, Tokyo, Japan), high-resolution transmission electron microscopy (HRTEM, Tecnai G² F20 S-Twin at 200 kV field-emission electron gun in Schottky mode), and energy-dispersive X-ray (EDX) spectroscopy. For HRTEM imaging, a small amount of the solid powder was dispersed in alcohol and sonicated for 1 min, after which then the solution was drop-casted onto commercially available carbon-coated copper grids. Brunauer–Emmett–Teller (BET) measurements were performed using a Belcat-M instrument (BEL Company, Osaka, Japan), elemental compositions were investigated by inductively coupled plasma optical emission spectroscopy (ICP-OES, model Optima 8300, Perkin-Elmer), and Mn^{2+} concentrations of the supernatant solution after catalysis were determined by inductively coupled plasma mass spectrometry (ICP-MS, MS Perkin-Elmer ELA DRC-e).

2.3. Confirmation of Catalytic Activities. The catalytic activities of the as-prepared control amorphous manganese oxide nanopowders, hollow a:MONTs, c:MONTs, and heat-treated crystalline manganese oxide nanoclusters were studied to evaluate their effectiveness in removing RhB from aqueous solution at ambient conditions. A 0.05 mM dye stock solution was prepared by dissolving 0.024 g of RhB (Sigma-Aldrich, Seoul, South Korea) in 1000 mL of DI water (in a volumetric flask) and stirred for 30 min. Then, 10 mL of the dye stock solution was placed in 50 mL beakers and 0.005-g solid samples were added. The mixtures (dye solution and solid samples) were stirred for 15 min under visible light at ambient conditions and pH 5 (obtained by a pH meter, WTW, Weilheim in Oberbayern, Germany) and then left to settle for 10 min. The mixtures were then centrifuged twice at 5000 rpm for 10 min. The centrifuged solutions (supernatants) were kept in the dark before analysis with a UV–vis spectrophotometer (Shimadzu UV-160A) to observe the dye-degradation effect. A control sample was also prepared for comparison; it consisted of a 0.05

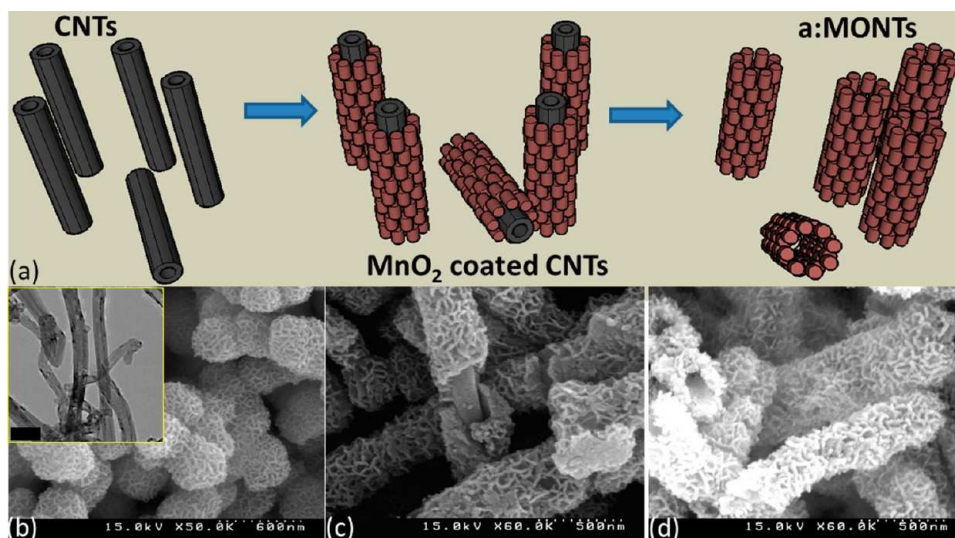
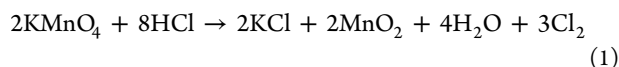


Figure 1. (a) Schematic view of a:MONTs formation and (b–d) SEM images of (b) amorphous manganese oxide nanoparticles, (c) amorphous manganese oxide-coated CNTs, and (d) hollow a:MONTs. The inset in panel b shows a TEM image of MWCNT templates (scale bar = 200 nm).

mM RhB solution (pH 5) subjected to magnetic stirring (under visible light for 15 min) with no catalyst.

3. RESULTS AND DISCUSSION

Figure 1a presents a schematic of the formation mechanism of hollow a:MONTs with the CNT-template method. First, the functionalized MWCNTs were coated with a manganese oxide layer according to the following reaction between KMnO_4 and HCl



Subsequent heat treatments ($400\text{ }^\circ\text{C}$) of the coated samples led to the removal of CNT templates, yielding hollow a:MONTs. It is important to note that the walls of the resulting a:MONTs were found to be highly porous. The formation of manganese oxide nanomaterial (reaction 1) was very rapid, with the evolution of gaseous byproducts, leading to a porous structure, as obtained for the control experiment shown in Figure 1b. This figure reveals that the as-synthesized amorphous manganese oxide nanoparticles (without using CNT templates) had highly porous surfaces and, thus, became porous nanotubes when coated on the CNT surface. Therefore, it is clear that this synthesis process is very fast, simple, and cost-effective for preparing hollow a:MONTs with porous walls. The inset of Figure 1b shows the MWCNT templates (as-received). Panels c and d of Figure 1 present the SEM images of manganese oxide-coated CNTs and hollow a:MONTs (after the removal of the CNT template), respectively. The figures clearly indicate the formation of hollow a:MONTs with uniform diameters. Obviously, the inner diameter of the hollow a:MONTs is defined by the diameter of the CNT templates used. The outer diameter, or the thickness of the walls of the hollow nanotubes, can be controlled by changing the manganese-to-carbon molar ratio in the precursor solution during coating, as discussed below.

The as-prepared a:MONTs were further heat-treated at higher temperatures to observe the crystalline phase and morphology of the nanotubes. Figure 2a presents the XRD traces of various heat-treated and untreated samples. Trace 1 of Figure 2a shows the XRD pattern of the amorphous manganese

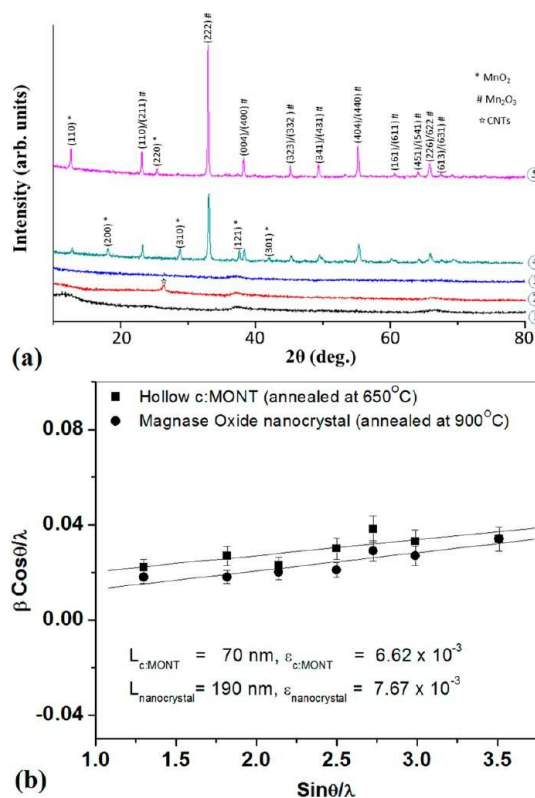


Figure 2. (a) XRD patterns of various manganese oxide nanostructures. (b) Size–strain analyses of c:MONT and crystalline manganese oxide nanoparticles.

oxide (MnO_2) nanoparticles, obtained in the control experiment. Trace 2 of Figure 2a shows the XRD pattern of amorphous manganese oxide-coated CNT samples, whereas trace 3 of Figure 2a presents the same for hollow a:MONTs after the removal of the CNTs at $400\text{ }^\circ\text{C}$. All three traces show no preferential crystalline manganese oxide peaks, indicating the typical amorphous nature of the nanostructures. When the hollow a:MONT samples were further heat-treated at $600\text{ }^\circ\text{C}$, the a:MONTs are converted into c:MONTs, keeping the porosity of the walls intact (the corresponding SEM images are

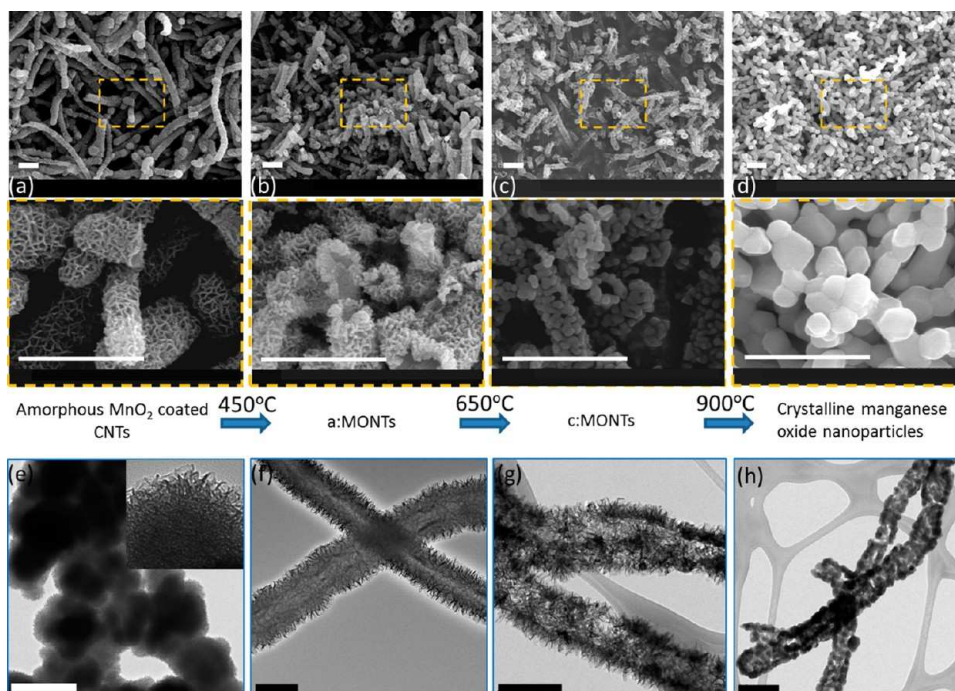


Figure 3. (a–d) SEM images (scale bars = 1 μm) of the effect of sequential heat treatments on the morphology of manganese oxide nanostructures (Mn-to-C molar ratio = 0.5), with magnifications of selected portions (dashed squares) shown immediately below the corresponding low-magnification images. (e–h) TEM images (scale bars = 400 nm) presenting the microstructures of (e) control amorphous manganese oxide nanoparticles, (f) amorphous manganese oxide-coated CNTs, (g) hollow a:MONTs, and (h) hollow c:MONTs. The inset in panel e presents a magnified view of one of the control amorphous manganese oxide nanoparticles.

shown later). Trace 4 of Figure 2a presents the XRD pattern of the corresponding hollow c:MONT samples. The XRD data analysis revealed that the crystallinity of the material was dominated by the Mn_2O_3 phase, along with a small fraction of cryptomelane MnO_2 (1999 JCPDS-ICDD card nos. 73-1826 and 72-1982). When these c:MONTs were further annealed at 900 $^\circ\text{C}$, the crystallinity of the samples was found to increase through an enhancement of the Mn_2O_3 peak intensities (cf. trace 5 of Figure 2a), along with the disappearance of some of the cryptomelane MnO_2 peaks. A previous report on temperature-dependent structural studies of manganese oxides with mixed phases showed that the cryptomelane MnO_2 phase is highly unstable under heat treatment above 600 $^\circ\text{C}$. When annealing is performed in ambient atmosphere, thermodynamically, mixed phase formation is more probable, but cryptomelane would be less stable at higher temperature. Hence, we obtained very small MnO_2 peaks that were less than 10% of the Mn_2O_3 phase, indicating a dominant Mn_2O_3 structure. Previously, Ghodbane et al. also reported similar mixed phase formation of manganese oxide microstructures under various heat treatments.⁴² On the other hand, the morphology of the crystalline nanostructure was observed to change from hollow nanotubes to nanoparticles through the collapse of the tubular structure (corresponding SEM images are shown later in Figure 3). This is mainly because of the strain generated in the tubular structure with the increments in the crystallinity and crystallite size with the dominant Mn_2O_3 phase, leading to the breakdown of the hollow nanotubes to nanoparticles. To further justify this explanation, size–strain analyses of the c:MONTs and nanoparticles were performed using the XRD data with the equation⁴³

$$\frac{\beta \cos \theta}{\lambda} = \frac{1}{L} + \frac{\epsilon \sin \theta}{\lambda} \quad (2)$$

where β is the full-width at half maximum (in radians) of the diffractions peaks of the Mn_2O_3 phase; θ is the corresponding diffraction angle; L and ϵ are the crystallite size and strain, respectively, of the nanomaterial; and λ is the X-ray wavelength used for XRD measurements (1.5405 \AA). A plot of $(\beta \cos \theta)/\lambda$ versus $(\sin \theta)/\lambda$ is thus a straight line, with its intercept and slope carrying information on the crystallite size and strain, respectively, of the nanomaterials. Figure 2b presents the size–strain analyses of the nanomaterials annealed at 600 and 900 $^\circ\text{C}$. The linear fitting of the data with a 10% error estimation revealed that, for c:MONTs, the crystallite size and strain were 70 ± 7 nm and $(6.62 \pm 0.7) \times 10^{-3}$, respectively, whereas for the collapsed nanoparticles, the crystallite size was found to be more than 100 nm (~ 190 nm, revealed by SEM images shown in Figure 3) with a strain of around $(7.67 \pm 0.8) \times 10^{-3}$, respectively. Clearly, the increment in the strain leads to the collapse of the nanotubes to nanoparticles. The increase in the crystallite size of the collapsed nanocrystals against c:MONTs is considered to have a significant effect on this structural breakdown, as the particle size of the collapsed structure (~ 200 nm) becomes comparable to the radial dimension of the c:MONTs (~ 250 nm, shown in Figure 3). It is to be noted that, in general, when nanomaterials (especially nanoparticles) are annealed at higher temperature, the nanocrystals tend to grow, leading to a more uniform morphology, followed by a release in strain. However, in the current case, because of the tubular geometry of the hollow c:MONTs, the growth of the nanocrystals at the tube walls increased the overall strain within the nanomaterial. Hence, we observed a broadening of the diffraction peaks, which is due to the generation of nonuniform

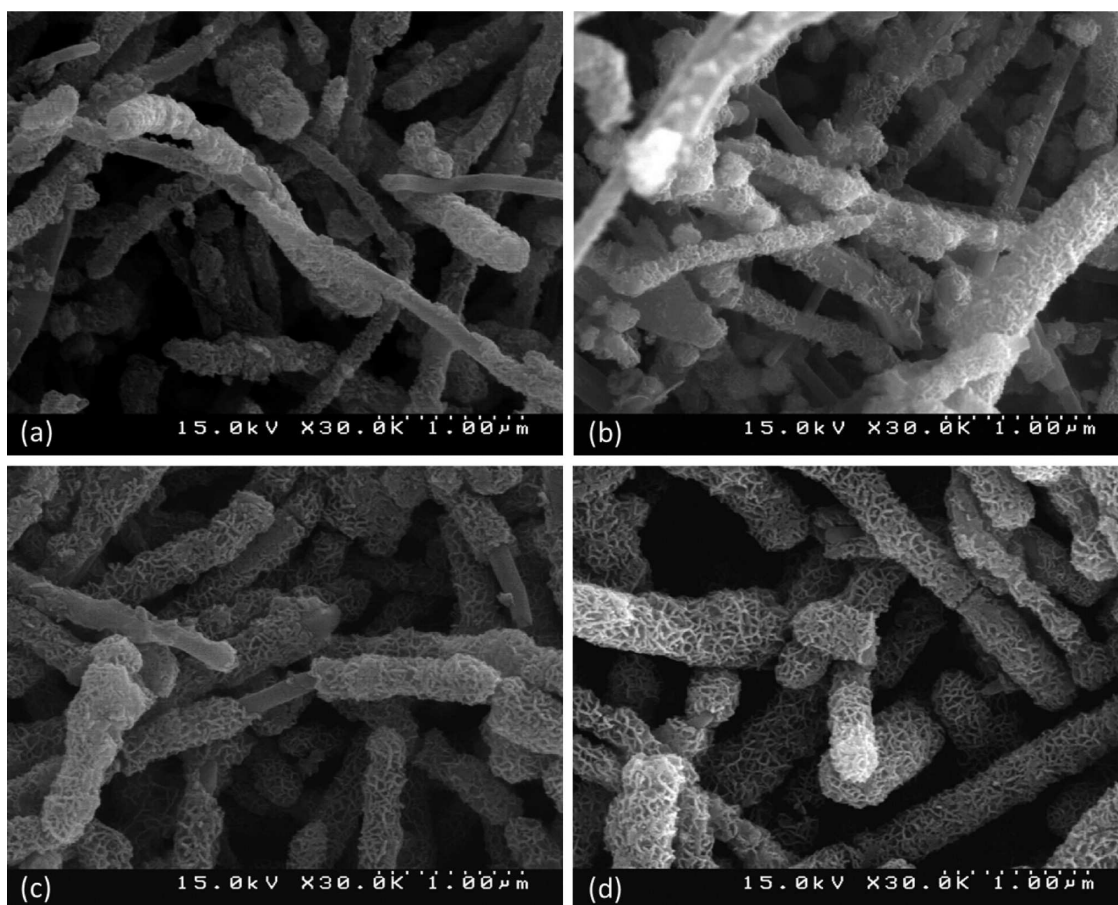


Figure 4. Effect of the Mn-to-C molar ratio in the precursor solution on the morphology of amorphous manganese oxide-coated CNTs for Mn-to-C molar ratios of (a) 0.2, (b) 0.25, (c) 0.33, and (d) 0.5.

strain.⁴⁴ Also, we observed a low- 2θ shift of the diffraction peaks of crystalline manganese oxide nanoparticles against hollow c:MONTs. For example, the 2θ value of the (222) peak of the c:MONTs ($2\theta_{\text{c:MONT}}^{(222)} = 33.1^\circ$) was found to shift to a lower value ($2\theta_{\text{c:NP}}^{(222)} = 32.87^\circ$) for crystalline nanoparticles (c:NP), indicating the generation of some uniform tensile strain within the nanostructures under heat treatment.⁴⁴ Similar shifts were observed for the other peaks as well. Apparently, the growth of nanocrystals at the tube walls generates some radially outward stress, leading to tensile strain. Obviously, for a freely growing oxide at ambient pressure, generation of both nonuniform and uniform strain is thermodynamically more probable and is reflected by changes in both the β and 2θ values. Additionally, as the size–strain analysis was performed taking into account all of the diffractions peaks (cf. eq 2), rather than individual peaks as is done by standard Scherer calculations, the instrumental broadening was suppressed. This is because, assuming that the XRD peaks have a Lorentzian (Cauchy) profile (which leads to a linear contribution of instrumental broadening to the total broadening) and considering that $\cos \theta$ is a slowly varying function in our operating range of 2θ , the instrumental broadening effect will mostly shift the size–strain plot along the vertical axis without changing the slope to a significant extent.⁴⁵ Thus, it might induce some errors in the crystallite size calculations, but it would not affect the strain calculations significantly.

The temperature-dependent sequential changes in the morphology and phase of the nanomaterial are depicted in

Figure 3 for clarity. The figure clearly shows the formation of amorphous manganese oxide-coated CNTs (cf. Figure 3a), which is converted into hollow a:MONTs after heat treatment at 400°C through the removal of CNT templates (cf. Figure 3b). The amorphous manganese oxide was found to be highly porous and to have a worm-like surface morphology. As a result, the walls of the hollow a:MONTs also became highly porous. Further heat treatment of these samples at 600°C converted the hollow a:MONTs into hollow c:MONTs (cf. Figure 3c). Because of the transition of the nanomaterial from amorphous to crystalline, the worm-like morphology was found to convert into granular nanocrystals, with the porosity of the walls retained. With further heat treatment of the samples at 900°C , the nanocrystals started to grow further with dimensions comparable to the diameters of the nanotubes, and thus the tubular structures collapsed to form agglomerated crystalline nanoparticles (cf. Figure 3d). TEM image of the control amorphous manganese oxide nanoparticles shows porous morphology (cf. Figure 3e and inset), which is transferred to the coating layers of CNTs, and hence the manganese oxide-coated CNTs also show highly porous structure (cf. Figure 3f). Figure 3g shows the TEM image of 400°C heat-treated samples, indicating the removal of CNT templates to form hollow a:MONTs with porous walls. Figure 3h shows the hollow c:MONTs, upon further heat treatment (600°C). The phase transformation from an amorphous worm-like morphology to a crystalline granular morphology is clearly visible. From the SEM and TEM images of Figure 3, it is

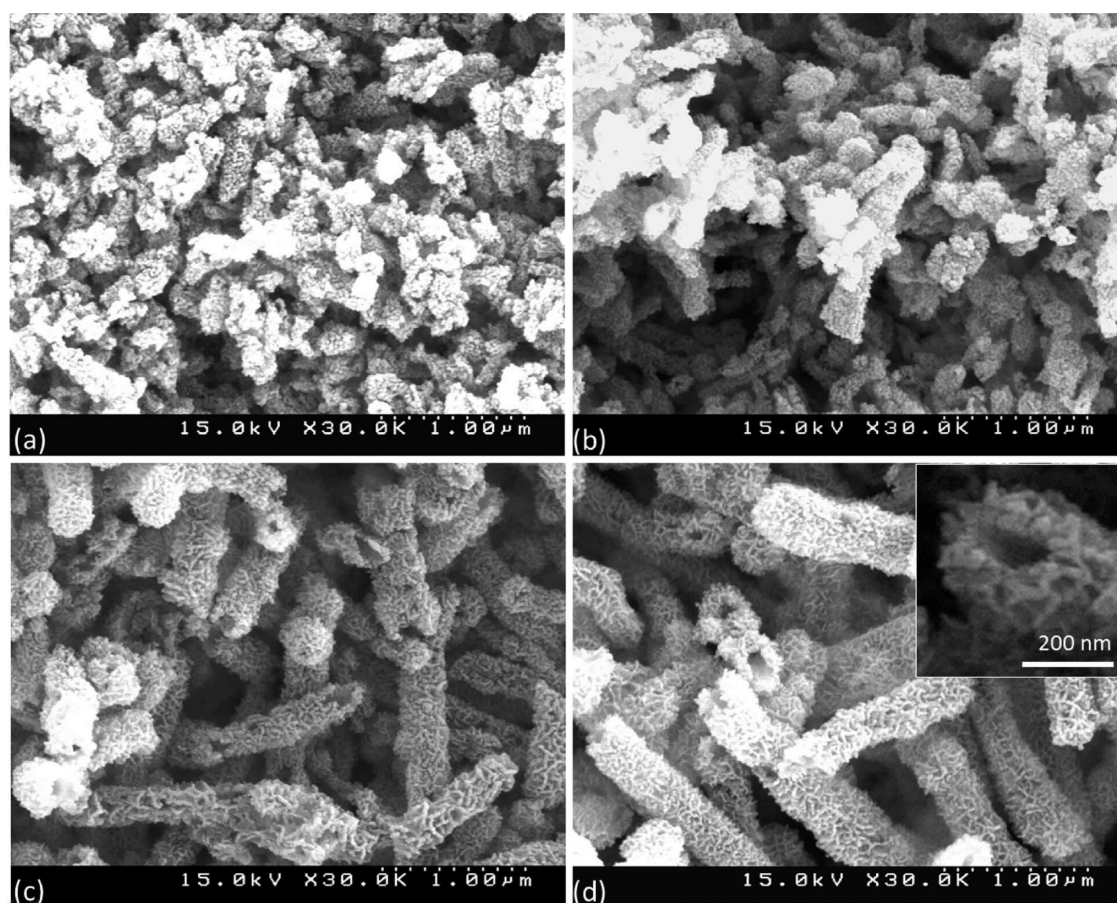


Figure 5. Effect of the Mn-to-C molar ratio on the morphology of heat-treated (at 450 °C for 15 h) amorphous manganese oxide nanotubes for Mn-to-C molar ratios of (a) 0.2, (b) 0.25, (c) 0.33, and (d) 0.5.

obvious that hollow a:MONTs have the highest porosity, followed by amorphous nanoparticles, hollow c:MONTs, and crystalline nanoparticles. The active specific surface areas of these nanostructures can be summarized in decreasing order as follows: hollow a:MONTs > amorphous manganese oxide nanoparticles > hollow c:MONTs > crystalline manganese oxide nanoparticles. This argument is supported by Brunauer–Emmett–Teller (BET) surface area measurements of the samples. The specific surface areas of these materials were found to be in the same decreasing order as stated above. For example, the BET specific surface areas for hollow a:MONTs, amorphous manganese oxide nanoparticles, hollow c:MONTs and crystalline manganese oxide nanoparticles are obtained as 190.42, 126.28, 67.35, and 41.07 m²/g, respectively. Also, BET adsorption–desorption plots of various manganese oxide nanostructures are presented in the Supporting Information (Figures S1–S4), along with a table (Table S1) comparing the BET surface areas, average pore sizes, and total pore volumes of different manganese oxide nanostructures. The table reveals that, although the average pore diameter of hollow a:MONTs was higher than that of other nanostructures, the BET surface area and total pore volume were also higher, indicating the contribution of larger inner tube pores (in addition to the smaller pores at the walls) to the total pore volume and BET surface area. Similarly, the larger inner tube pores of the hollow c:MONTs also contribute to the higher values of their total pore volume and BET surface area against crystalline manganese oxide nanoparticles. The effects of the variations

in the active surface areas of these nanostructures on the corresponding catalytic activities are discussed later.

Additionally, to find the elemental compositions of the amorphous and crystalline samples (especially the amounts of residual K and Cl), inductively coupled plasma optical emission spectrometry (ICP-OES) measurements were performed, and the data are presented in the Supporting Information (Table S2). The table reveals that, with the heat treatment, both the percentage of residual potassium and chlorine decrease within the samples.

Figure 4 shows SEM images of amorphous manganese oxide-coated CNTs with different ratios of the coating material and the template. To be specific, we varied the Mn-to-C molar ratio in the precursor solution to observe its effect on the efficiency and uniformity of the coating on the CNT template. At a very low Mn-to-C molar ratio (0.2), partially coated CNTs with amorphous manganese oxides formed (cf. Figure 4a). With a further increase in the Mn-to-C molar ratio to 0.25 and 0.33, larger coverage of the CNT surfaces was observed with higher uniformity, although discontinuities in the coating were also observed in some regions (Figure 4b,c). When the Mn-to-C molar ratio in the precursor solution was further increased to 0.5, complete coverage of the CNT surfaces with a highly uniform coating was observed (Figure 4d). The EDX analyses of all of these samples, shown in Figure 4, depict a gradual increase in the Mn-to-C elemental ratio (0.19, 0.24, 0.31, and 0.43, respectively) in the as-fabricated nanostructures, which is

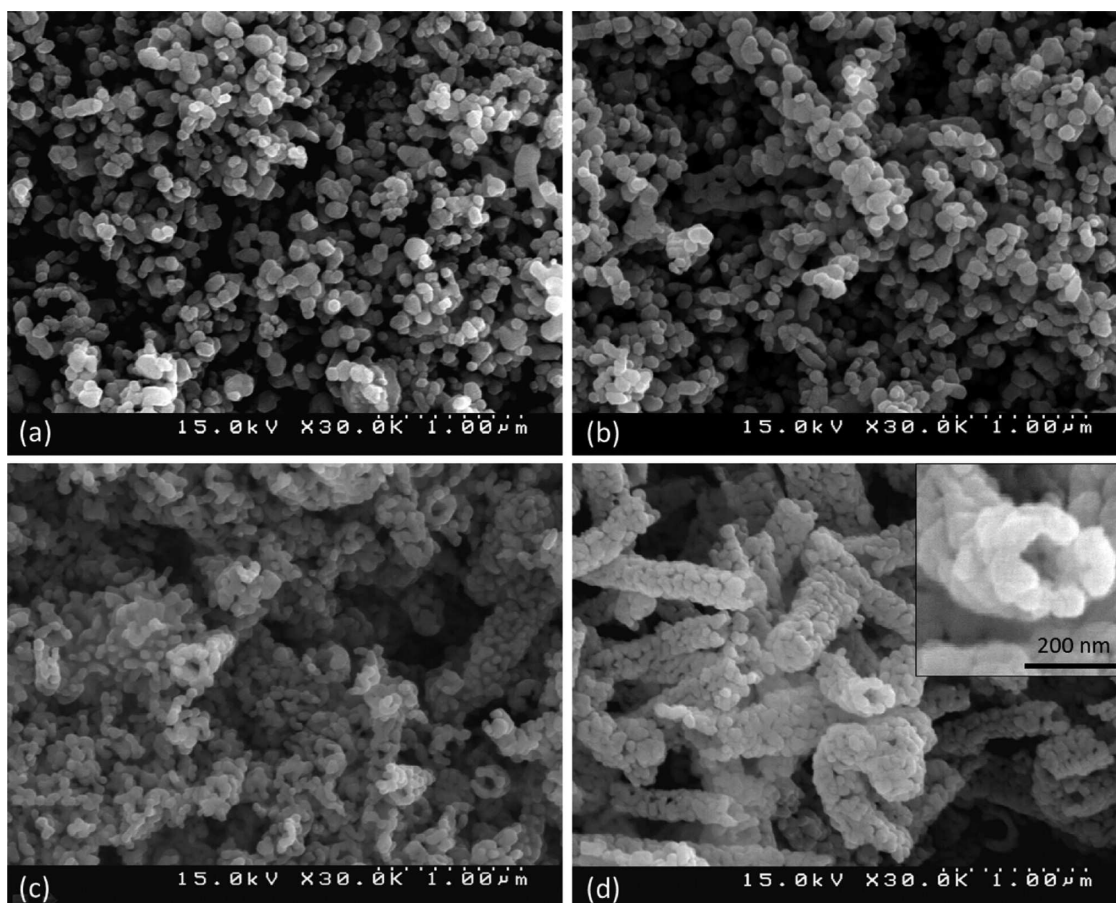


Figure 6. Effect of the Mn-to-C ratio on the morphology of heat-treated (at 650 °C for 15 h) crystalline manganese oxide nanotubes for Mn-to-C ratio (a) 0.2, (b) 0.25, (c) 0.33, and (d) 0.5.

in accordance with the proportional increase of the Mn-to-C molar ratio in the precursor solution described above.

Because the coating efficiency and uniformity depend on the Mn-to-C molar ratio, the morphologies of the corresponding heat-treated samples (400 °C) were also strongly affected by this ratio. At a lower value of the Mn-to-C molar ratio in the precursor solution (0.2), as the coating was discontinuous, it collapsed to form nanoclusters after the removal of the CNT templates (cf. Figure 5a). At a higher value of the Mn-to-C molar ratio of 0.25, a mixture of nanoclusters and hollow nanotubes formed because only a small fraction of the CNT templates were coated with continuous manganese oxide layers (cf. Figure 5b). With a further increase in the Mn-to-C molar ratio to 0.33, as the coating became more continuous, a higher percentage of hollow a:MONTs formed with respect to nanoclusters (cf. Figure 5c), although the thickness of the nanotube walls was comparatively lower (~20 nm). Finally, for a Mn-to-C molar ratio of 0.5, as the coating was highly uniform and continuous, the complete formation of hollow a:MONTs was observed after the removal of the CNT templates under annealing at 400 °C (cf. Figure 5d). The inset of Figure 5d presents a magnified view of the cross section of a hollow a:MONT. The figure reveals that the average inner diameter of the hollow nanotubes was around 150 nm (defined by the diameter of the CNT template used, which was also around 150 nm, as shown in the inset of Figure 1b), and the outer diameter was around 250 nm, indicating a wall thickness of ~50 nm. Also, the nanotube walls were found to be highly porous, thus

indicating a very high specific surface area for interesting interfacial and surface-related applications.

These amorphous nanostructures (shown in Figure 5), fabricated at four different Mn-to-C molar ratios, when further heat-treated at 600 °C, were found to convert into crystalline manganese oxide nanostructures with a dominant Mn_2O_3 phase. The XRD pattern was observed to be identical to that present in trace 4 of Figure 2a. At lower Mn-to-C molar ratios (0.20, 0.25), agglomerated nanocrystals formed with an average dimension of 100 nm (cf. Figure 6a,b). For the amorphous nanostructure having a Mn-to-C molar ratio 0.33, a mixture of very short c:MONTs and agglomerated nanocrystals formed (cf. Figure 6c) under heat treatment (600 °C). The percentage of nanotubes was found to be much less than the percentage of nanoclusters in this case. This is because the corresponding hollow amorphous nanotubes (shown in Figure 5c) had very low wall thicknesses (~10–20 nm) and thus collapsed under heat treatment. In the case of amorphous nanotubes fabricated at a Mn-to-C molar ratio of 0.5, the wall thickness was found to be higher (~50 nm, as shown in the inset of Figure 5d), and these nanostructures were observed to withstand the heat treatment effectively to convert completely into hollow c:MONTs without collapsing. A closer examination of the cross section of the c:MONTs (inset of Figure 6d) revealed that the inner and outer diameters were similar to those obtained for a:MONTs (cf. inset of Figure 5d). This indicates that the heat treatment at 600 °C basically causes a phase transition of manganese oxide from amorphous to crystalline, as well as a change in the surface morphology from an amorphous

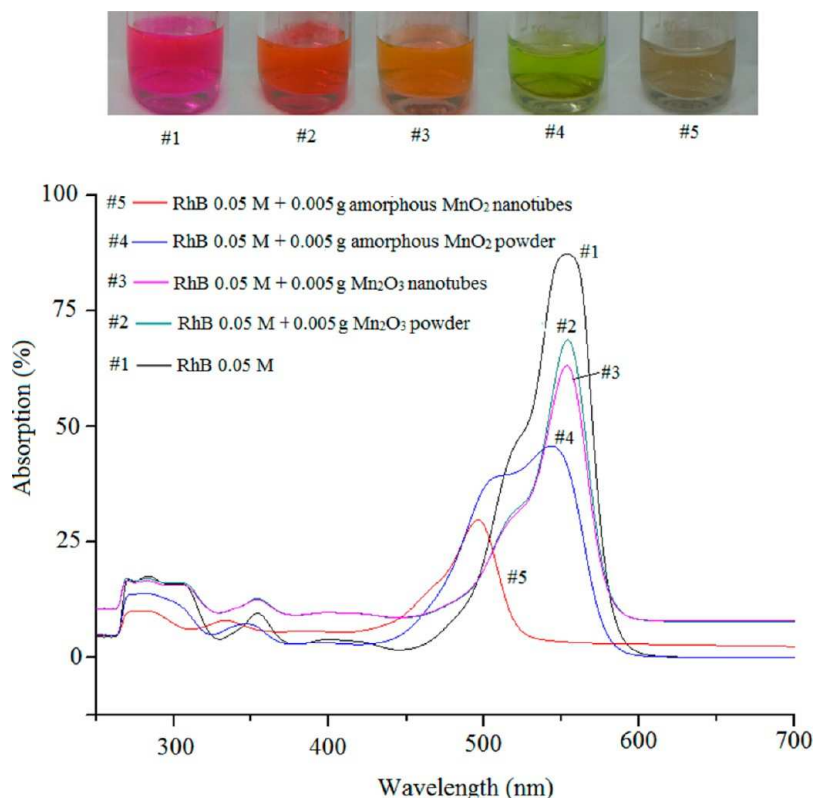


Figure 7. UV–vis absorption spectra of catalytically degraded RhB solution treated with different manganese oxide nanostructures.

worm-like structure to a crystalline granular structure, keeping the porosity intact.

Although a higher Mn-to-C molar ratio gives more uniform hollow nanotubes, there exists an optimum ratio for efficient coating on the CNT templates. When the Mn-to-C molar ratio was very high (around 2.5), instead of coating the CNT templates, amorphous manganese oxide nanoparticle formed within the reaction volume, with dispersed CNTs inside the amorphous manganese oxide matrix, as shown in Figure S7 of the Supporting Information. Under our experimental conditions, an Mn-to-C-molar ratio of 0.5 was found to produce the most efficient coating of CNT templates, which were converted effectively into hollow a:MONTs and c:MONTs under subsequent heat treatments. Also, the effects of sequential heat treatments of manganese oxide-coated CNT templates prepared at various Mn-to-C molar ratios are summarized in Figure S8 of the Supporting Information. Clearly, a higher Mn-to-C molar ratio produces highly uniform a:MONTs and c:MONTs with porous walls. Also, 600 °C was found to be an optimum temperature under our experimental conditions, above which the tubular structure collapsed into agglomerated nanocrystals. A magnified view of the high-resolution TEM image of one of the granular crystals of c:MONT (shown in Figure S9 of the Supporting Information) displays the very high crystallinity of the nanomaterial. A selected-area electron diffraction pattern (inset of Figure S9, Supporting Information) also corroborates the result.

The catalytic performances of the amorphous manganese oxide nanoparticles (prepared in a control experiment), as-synthesized hollow a:MONTs, hollow c:MONTs, and crystalline manganese oxide nanoparticles (prepared at 900 °C) were evaluated through the degradation of RhB in aqueous solution,

and the comparative degradation efficiencies were measured by UV–vis absorption spectroscopy. Figure 7 presents the absorption spectra of different nanostructures mentioned above. Curve 1 of this figure shows the reference spectrum of the stock dye solution without catalytic treatment. Curves 2 and 4 represent the RhB solution degraded catalytically with crystalline manganese oxide nanoparticles (which had a dominant Mn_2O_3 phase, cf. Figure 2) and amorphous manganese oxide nanoparticles (obtained by control experiment), respectively. Similarly, curves 3 and 5 represent the same under catalytic treatments of hollow c:MONTs and a:MONTs, respectively. The relative peak intensities reveal that amorphous hollow a:MONTs have the highest catalytic degradation efficiency followed by amorphous manganese oxide nanoparticles. A quantitative analysis of the catalytic performances of the various manganese oxide nanostructures was performed by measuring the relative decrease in dye concentration at a subsequent time against the initial value by estimating the peak absorbance of the absorption spectra of the dye solution according to the relation⁴⁶

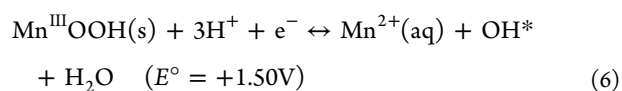
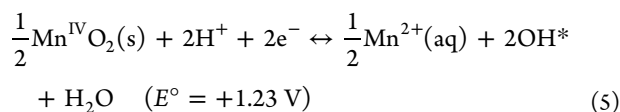
$$d(\%) = \left(1 - \frac{a_{\text{dye}}^{\tau}}{a_{\text{dye}}^0} \right) \times 100 \quad (3)$$

where d is the percentage relative dye degradation and a_{dye}^0 and a_{dye}^{τ} are the peak absorbances of the dye solution at its initial concentration and after catalysis for time τ , respectively. In the current case, after 15 min of catalytic degradation of RhB dye solution with different manganese oxide nanostructures, the degradation was found to be 70% for hollow a:MONTs, 50% for amorphous manganese oxide nanoparticles, 30% for hollow c:MONTs, and 20% for crystalline manganese oxide nanoparticles, indicating better catalytic performance of hollow

a:MONTs over other manganese oxide nanostructures. Also, at low dye concentrations, the Langmuir–Hinshelwood model of degradation kinetics can be approximated as an apparent first-order kinetic reaction according to the relation⁴⁷

$$\ln\left(\frac{c_{\text{dye}}^{\tau}}{c_{\text{dye}}^0}\right) = -\kappa_{\text{app}}\tau \quad (4)$$

where c_{dye}^0 and c_{dye}^{τ} are the dye concentrations at the initial time and after catalysis for time τ , respectively, and κ_{app} is the apparent first-order rate constant. Therefore, a plot of $\ln(c_{\text{dye}}^{\tau}/c_{\text{dye}}^0)$ versus degradation time (τ) of each catalyst should be a straight line, the slope of which represents the first-order rate constant. In the current case, the time effluence of the degradation plots of each catalyst (not shown here) shows a linear fit, and the calculations of κ_{app} for different manganese oxide nanostructures give values of 8.02×10^{-2} , $4.62 \times 10^{-2} \text{ min}^{-1}$, $^{-1}$ and $1.42 \times 10^{-2} \text{ min}^{-1}$ for hollow a:MONTs, amorphous nanoparticles, hollow c:MONTs, and crystalline nanoparticles, respectively. Now, considering the fact that all of the catalysts have different specific surface areas, the above-mentioned apparent rate constants are normalized with the corresponding BET surface areas (S_{BET}) to obtain the specific rate constant ($\kappa_{\text{sp}} = \kappa_{\text{app}}/S_{\text{BET}}$).⁴⁸ The values of κ_{sp} were obtained as 4.21×10^{-4} , 3.66×10^{-4} , 3.53×10^{-4} , and $3.46 \times 10^{-4} \text{ min}^{-1} \text{ g m}^{-2}$ for hollow a:MONTs, amorphous nanoparticles, hollow c:MONTs, and crystalline nanoparticles, respectively. The values of κ_{app} and κ_{sp} of different manganese oxide nanostructures are collected in the Supporting Information (Table S3). Clearly, both values indicated a monotonic decrease in the order hollow a:MONTs > amorphous nanoparticles > hollow c:MONTs > crystalline nanoparticles, indicating that the hollow a:MONTs had better catalytic activity than the other samples. Also, it is noteworthy that the calculated values of κ_{app} for the amorphous manganese oxide nanostructures were better than the reported values obtained from the catalytic dye degradation activities (having similar initial RhB concentrations) of other well-known catalysts such as TiO_2 .^{46,49} This is purely because of the porous morphology of these amorphous nanostructures, which offer much higher active surface area for improved catalytic activities (as shown in Figure 3). Apparently, the hollow a:MONTs with porous walls had relatively higher specific surface areas than the amorphous porous nanoparticles because of the hollow one-dimensional tubular structures with inner and outer active surfaces. On the other hand, the crystalline nanostructures (c:MONTs and crystalline nanoparticles) show lower catalytic performances than the amorphous nanostructures (a:MONTs and amorphous nanoparticles), as the corresponding absorption peaks were found to be higher than those of the amorphous structures. This is because Mn^{IV} (which is the dominant oxidation state of Mn in our amorphous oxide nanostructures) and Mn^{III} (which is the dominant oxidation state of Mn in the crystalline oxide nanostructures) are readily converted to Mn^{2+} state at $\text{pH} < 7$ to produce hydroxyl radicals (OH^*) according to the overall reaction schemes⁵⁰



where E° is the standard reduction potential. These released hydroxyl radicals then oxidize the RhB solution to degrade into CO_2 and nontoxic inorganic products.^{46,51} Because of the slight difference in the reduction potentials between Mn^{IV} and Mn^{III} , as well as the higher porosity of amorphous nanostructures, they offer higher surface reactions sites and, thus, show better catalytic performance than crystalline nanostructures. Regarding the relative catalytic performances of crystalline nanostructures, c:MONTs showed better dye degradation than crystalline nanoparticles because of their smaller crystallite size (~ 70 vs 190 nm for crystalline nanoparticles, cf. Figure 2b) and hollow tubular structure with porous walls to offer larger surface-to-volume ratio, resulting in higher reactive surface sites. These results were also corroborated by BET surface area measurements, discussed earlier, where the specific surface areas of the nanostructures were found to be in decreasing order hollow amorphous manganese oxide nanotubes > amorphous manganese oxide nanoparticles > hollow crystalline manganese oxide nanotubes > crystalline manganese oxide nanoparticles, thus supporting the relative catalytic activities of these nanostructures. Additionally, the proposed mechanism of leaching of Mn^{2+} from the catalyst into the solution, followed by hydroxyl radical formation (as described in eqs 5 and 6), was corroborated by the chemical analysis of the supernatant solution after the removal of catalysts. The ICP-MS data are available in the Supporting Information (Table S4), which reveals that the solution treated with a:MONTs had the highest Mn^{2+} concentration, followed by the amorphous nanoparticles (a:NPs), c:MONTs, and crystalline nanoparticles (c:NPs), respectively. The presence of a very small amount of Mn^{2+} in the control solution (stock dye solution before catalysis) was due to some impurities within the dye. However, after catalysis, solutions treated with crystalline MnO_2 nanostructures showed a 4-fold increment in the Mn^{2+} concentrations to as high as a 44-fold increment compared to those treated with a:MONTs (cf. Table S4, Supporting Information). Clearly, the trend is in accordance with the degradation curve given in Figure 7, thus supporting our proposed mechanism.

We also observed a baseline drift of the absorption curves with respect to the reference curve (curve 1). We presume that this increase in the baseline is due to the self-degradation of the catalysts according to the reactions schemes presented in eqs 5 and 6, where the RhB degradation is proposed to be due to the leaching of Mn^{2+} from the catalysts to the solution followed by hydroxyl radicals (OH^*) formation. Previously, a similar baseline drift of RhB degradation curves under H_2O_2 -activated FePcCl_{16} photocatalysts was reported by Wang et al., who argued that the photocatalysts were self-degraded under H_2O_2 environment to produce the baseline drift.⁵²

4. CONCLUSIONS

Novel nanostructures in the form of amorphous and crystalline hollow manganese oxide nanotubes with porous walls have been fabricated for the first time by a very simple and cost-effective method. Carbon nanotubes were first coated with amorphous manganese oxide layers by the acidic reduction of KMnO_4 under ambient conditions. Carbon nanotubes were used as sacrificial templates, and heat treatments (at 400°C) of these nanocomposites resulted in the removal of carbon

nanotubes to form hollow manganese oxide nanotubes. The rapid reaction process along with the evolution of gaseous byproducts allowed for the formation of porous walls of the hollow nanotubes. The XRD analysis revealed that the hollow nanotubes were amorphous in nature and converted into crystalline hollow manganese oxide nanotubes with a dominant Mn_2O_3 phase when heat-treated at 600 °C. SEM and TEM analyses further confirmed the formation of hollow nanotubes with porous worm-like morphologies in amorphous nanotubes and granular morphologies in crystalline nanotubes. The catalytic activities of these nanostructures in terms of the degradation of an organic dye (rhodamine B) solution, as well as BET surface area measurements, revealed that hollow amorphous manganese oxide nanotubes provided the highest surface reaction sites because of their porous hollow tubular structures. The successful fabrication of amorphous and crystalline hollow manganese oxide nanotubes with porous walls offers very high specific surface areas for promising applications not only in water pollutant treatment but also in energy storage, solar cells, supercapacitors, and giant magneto-resistance devices, among others.

■ ASSOCIATED CONTENT

● Supporting Information

BET adsorption/desorption plots and pore size and pore volume data for hollow a:MONTs, amorphous manganese oxide nanoparticles, hollow c:MONTs, and crystalline manganese oxide nanoparticles (Figures S1–S4, Table S1); ICP-OES (inductively coupled plasma optical emission spectrometry analysis data for MnO_2 samples before and after heat treatment (Table S2); dispersed CNTs inside amorphous manganese oxide matrix for a Mn-to-C molar ratio of 2.5 (Figure S5); overall sequential modification of manganese oxide nanostructures as a function of annealing temperature and Mn-to-C molar ratio (Figure S6); HRTEM image of one of the granular crystals of c:MONT for a Mn-to-C molar ratio of 0.5 (Figure S7); apparent and specific rate constants of various manganese oxide nanostructures (Table S3), and ICP-MS analysis data for supernatant solution after catalysis (Table S4). This material is available free of charge via the Internet at <http://pubs.acs.org>.

■ AUTHOR INFORMATION

Corresponding Authors

*Fax: +82 53 810 2062. Tel.: +82 53 810 2568. E-mail: swjoo@ynu.ac.kr

*Fax: +82 53 810 2062. Tel.: +82 53 810 2453. E-mail: arghya@ynu.ac.kr, banerjee_arghya@hotmail.com.

Notes

The authors declare no competing financial interest.

■ ACKNOWLEDGMENTS

This work was funded by Vietnam's National Foundation for Science and Technology Development (NAFOSTED) (Project 103.02-2013.76) and World Class University Grant R32-2008-000-20082-0 of the National Research Foundation of Korea. We also thank Professor M. A. Cheney of University of Maryland for insightful discussions.

■ REFERENCES

(1) Lieber, C. M.; Wang, Z. L. Functional Nanowires. *Mater. Res. Bull.* **2007**, *32*, 99–104.

(2) Remskar, M. Inorganic Nanotubes. *Adv. Mater.* **2004**, *16*, 1497–1504.

(3) Xia, X.; Tu, J.; Zhang, Y.; Wang, X.; Gu, C.; Zhao, X.; Fan, H. J. High-Quality Metal Oxide Core/Shell Nanowire Arrays on Conductive Substrates for Electrochemical Energy Storage. *ACS Nano* **2012**, *6*, 5531–5538.

(4) Fan, H. J.; Gosele, U.; Zacharias, M. Formation of Nanotubes and Hollow Nanoparticles Based on Kirkendall and Diffusion Process: A Review. *Small* **2007**, *3*, 1660–1671.

(5) Liao, M. Y.; Huang, C. C.; Chang, M. C.; Lin, S. F.; Liu, T. Y.; Su, C. H.; Yeh, C. S.; Lin, H. P. Synthesis of Magnetic Hollow Nanotubes Based on the Kirkendall Effect for MR Contrast Agent and Colorimetric Hydrogen Peroxide Sensor. *J. Mater. Chem.* **2011**, *21*, 7974–7981.

(6) Ortiz, G. F.; Lopez, M. C.; Alcantara, R.; Tirado, J. Electrodeposition of Copper–Tin Nanowires on Ti Foils for Rechargeable Lithium Micro-Batteries with High Energy Density. *J. Alloys Compd.* **2014**, *585*, 331–336.

(7) Jia, B.; Gao, L. Morphological Transformation of Fe_3O_4 Spherical Aggregates from Solid to Hollow and Their Self-Assembly under an External Magnetic Field. *J. Phys. Chem. C* **2008**, *112*, 666–671.

(8) Lu, X.; Au, L.; McLellan, J.; Li, Z. Y.; Marquez, M.; Xia, Y. Fabrication of Cubic Nanocages and Nanoframes by Dealloying Au/Ag Alloy Nanoboxes with an Aqueous Etchant Based on $\text{Fe}(\text{NO}_3)_3$ or NH_4OH . *Nano Lett.* **2007**, *7*, 1764–1769.

(9) Yin, Y.; Rioux, R. M.; Erdonmez, C. K.; Hughes, S.; Somorjai, G. A. A.; Alivisatos, P. Formation of Hollow Nanocrystals through the Nanoscale Kirkendall Effect. *Science* **2004**, *340*, 711–714.

(10) Hong, J. F.; Knez, M.; Scholz, R.; Nielsch, E. P.; Hesse, D.; Zacharias, M.; Gosele, U. Monocrystalline Spinel Nanotube Fabrication Based on the Kirkendall Effect. *Nat. Mater.* **2006**, *5*, 627–631.

(11) Song, Z.; Liu, W.; Zhao, M.; Zhang, Y.; Liu, G.; Yu, C.; Qiu, J. A Facile Template-Free Synthesis of $\alpha\text{-MnO}_2$ Nanorods for Supercapacitor. *J. Alloys Compd.* **2013**, *560*, 151–155.

(12) Yang, T.; Zhang, Y.; Li, C. Chemical and Structural Analysis of Solvothermal Synthesized Tungsten Oxide Nanotube without Template and Its Hydrogen Sensitive Property. *J. Alloys Compd.* **2014**, *584*, 546–552.

(13) Korhonen, J. T.; Hiekkataipale, P.; Malm, J.; Karppinen, M.; Ikkala, O.; Ras, R. H. A. Inorganic Hollow Nanotube Aerogels by Atomic Layer Deposition onto Native Nanocellulose Templates. *ACS Nano* **2011**, *5*, 1967–1974.

(14) Huang, X.; Wang, M.; Willinger, M. G.; Shao, L.; Su, D. S.; Meng, X. M. Assembly of Three-Dimensional Hetero-Epitaxial ZnO/ZnS Core/Shell Nanorod and Single Crystalline Hollow ZnS Nanotube Arrays. *ACS Nano* **2012**, *6*, 7333–7339.

(15) Karki, K.; Zhu, Y.; Liu, Y.; Sun, C. F.; Hu, L.; Wang, Y. H.; Wang, C.; Cumings, J. Hoop-Strong Nanotubes for Battery Electrodes. *ACS Nano* **2013**, *7*, 8295–8302.

(16) Schieder, M.; Lunkenbein, T.; Martin, T.; Milius, W.; Auffermann, G.; Brey, J. Hierarchically porous tungsten oxide nanotubes with crystalline walls made of the metastable orthorhombic polymorph. *J. Mater. Chem. A* **2013**, *1*, 381–387.

(17) Huang, C. C.; Huang, W.; Yeh, C. S. Shell-by-Shell Synthesis of Multi-Shelled Mesoporous Silica Nanospheres for Optical Imaging and Drug Delivery. *Biomaterials* **2011**, *32*, 556–564.

(18) Sun, Y.; Zhang, L.; Wang, Y.; Chen, P.; Xin, S.; Jiu, H.; Liu, J. Hollow and Hollow Core/Shell $\text{CeO}_2/\text{SiO}_2@/\text{CeO}_2$ Spheres: Synthesis, Structure Evolution and Catalytic Properties. *J. Alloys Compd.* **2014**, *586*, 441–447.

(19) Milivojević, D.; Babić-Stojić, B.; Jokanović, V.; Jagličić, Z.; Makovec, D. Magnetic Properties of Mn-Oxide Nanoparticles Dispersed in an Amorphous SiO_2 Matrix. *J. Magn. Magn. Mater.* **2011**, *323*, 805–812.

(20) Kim, H. J.; Lee, J. B.; Kim, Y. M.; Jung, M. H.; Jagličić, Z.; Umek, P.; Dolinšek, J. Synthesis, Structure and Magnetic Properties of $\beta\text{-MnO}_2$ Nanorods. *Nanoscale Res. Lett.* **2007**, *2*, 81–86.

- (21) Wu, M. S.; Lee, J. T.; Wang, Y. Y.; Wan, C. C. Field Emission from Manganese Oxide Nanotubes Synthesized by Cyclic Voltammetric Electrodeposition. *J. Phys. Chem. B* **2004**, *108*, 16331–16333.
- (22) Kim, H. J.; Lee, J. B. Method for Manufacturing Manganese Oxide Nanotube or Nanorod by Anodic Aluminum Oxide Template. U.S. Patent 7,713,660, May 11, 2010.
- (23) Brock, S. L.; Duan, N.; Tian, Z. R.; Giraldo, O.; Zhou, H.; Suib, S. L. A Review of Porous Manganese Oxide Materials. *Chem. Mater.* **1998**, *9*, 2619–2628.
- (24) Truong, T. T.; Liu, Y.; Ren, Y.; Trahey, L.; Sun, Y. Morphological and Crystalline Evolution of Nanostructured MnO₂ and Its Application in Lithium–Air Batteries. *ACS Nano* **2012**, *6*, 8067–8077.
- (25) Golden, D. C.; Chen, C. C.; Dixon, J. B. Synthesis of Thodorokite. *Science* **1986**, *231*, 717–719.
- (26) Yang, Y.; Liu, E.; Li, L.; Huang, Z.; Shen, H.; Xiang, X. Nanostructured Amorphous MnO₂ Prepared by Reaction of KMnO₄ with Triethanolamine. *J. Alloys Compd.* **2010**, *505*, 555–559.
- (27) Moon, J.; Awano, M.; Takagi, H.; Fujishiro, Y. Synthesis of Nanocrystalline Manganese Oxide Powders: Influence of Hydrogen Peroxide on Particle Characteristics. *J. Mater. Res.* **1999**, *14*, 4594–4601.
- (28) Cai, J.; Liu, J.; Suib, S. L. Preparative Parameters and Framework Dopant Effects in the Synthesis of Layer-Structure Birnessite by Air Oxidation. *Chem. Mater.* **2002**, *14*, 2071–2077.
- (29) Cheney, M. A.; Bhowmik, P. K.; Moriuchi, S.; Villalobos, M.; Qian, S.; Joo, S. W. The Effect of Stirring on the Morphology of Birnessite Nanoparticles. *J. Nanomater.* **2008**, *2008*, No. 168716.
- (30) Xiao, T. D.; Strutt, P. R.; Benaissa, M.; Chen, H.; Kear, B. H. Synthesis of High Active-Site Density Nanofibrous MnO₂-Based Materials with Enhanced Permeabilities. *Nanostruct. Mater.* **1998**, *10*, 1051–1061.
- (31) Xiong, Y.; Xie, Y.; Li, Z.; Wu, C. Growth of Well-Aligned γ -MnO₂ Monocrystalline Nanowires through a Coordination-Polymer-Precursor Route. *Chem.—Eur. J.* **2003**, *9*, 1645–1651.
- (32) Wang, X.; Li, Y. Selected-Control Hydrothermal Synthesis of α - and β -MnO₂ Single Crystal Nanotubes. *J. Am. Chem. Soc.* **2002**, *124*, 2880–2881.
- (33) Qi, F. Synthesis and Application of Manganese Oxide Nanotubes. *Top. Appl. Phys.* **2010**, *117*, 73–82.
- (34) Chen, Z.; Yu, A. P.; Ahmed, R.; Wang, H. J.; Li, H.; Chen, Z. W. Manganese Dioxide Nanotube and Nitrogen-Doped Carbon Nanotube Based Composite Bifunctional Catalyst for Rechargeable Zinc-Air Battery. *Electrochim. Acta* **2012**, *69*, 295–300.
- (35) Xia, H.; Lai, M. O.; Lu, L. Nanoflaky MnO₂/Carbon Nanotube Nanocomposites as Anode Materials for Lithium-Ion Batteries. *J. Mater. Chem.* **2010**, *20*, 6896–6902.
- (36) Ma, S. B.; Nam, K. W.; Yoon, W. S.; Yang, X. Q.; Ahn, K. Y.; Oh, K. H.; Kim, K. B. Electrochemical Properties of Manganese Oxide Coated onto Carbon Nanotubes for Energy-Storage Applications. *J. Power Sources* **2008**, *178*, 483–489.
- (37) Chen, Y.; Zhang, Y.; Geng, D. S.; Li, R.; Hong, H. L.; Chen, J. Z.; Sun, X. L. One-Pot Synthesis of MnO₂/Graphene/Carbon Nanotube Hybrid by Chemical Method. *Carbon* **2011**, *49*, 4434–4442.
- (38) Mette, K.; Bergmann, A.; Tessonier, J. P.; Hävecker, M.; Yao, L.; Ressler, T.; Schlögl, R.; Strasser, P.; Behrens, M. Nanostructured Manganese Oxide Supported on Carbon Nanotubes for Electrocatalytic Water Splitting. *Chem. Catal. Chem.* **2012**, *6*, 851–862.
- (39) Sun, S.; Wang, W.; Sang, M.; Ren, J.; Zhang, L. Efficient Catalytic Oxidation of Tetraethylated Rhodamine over Ordered Mesoporous Manganese Oxide. *J. Mol. Catal. A: Chem.* **2010**, *320*, 72–78.
- (40) Cao, G.; Su, L.; Zhang, X.; Li, H. Hydrothermal Synthesis and Catalytic Properties of α - and β -MnO₂ Nanorods. *Mater. Res. Bull.* **2010**, *45*, 425–428.
- (41) Zheng, D.; Sun, S.; Fan, W.; Yu, H.; Fan, C.; Cao, G.; Yin, Z.; Song, X. One-Step Preparation of Single-Crystalline β -MnO₂ Nanotubes. *J. Phys. Chem. B* **2005**, *109*, 16439–16443.
- (42) Ghodbane, O.; Pascal, J. L.; Fraisse, B.; Favier, F. Structural in Situ Study of the Thermal Behavior of Manganese Oxide Materials: Toward Selected Electrode Materials for Supercapacitors. *ACS Appl. Mater. Interfaces* **2010**, *2*, 3493–3505.
- (43) Qadri, S. B.; Skelton, E. F.; Hsu, D.; Dinsmore, A. D.; Yang, J.; Gray, H. F.; Ratna, B. R. Size-Induced Transition-Temperature Reduction in Nanoparticles of ZnS. *Phys. Rev. B* **1999**, *60*, 9191–9193.
- (44) Cullity, B. D. *Elements of X-ray Diffraction*; Addison-Wesley: Reading, MA, 1978.
- (45) Suryanarayana, C.; Norton, M. G. *X-ray Diffraction: A Practical Approach*; Plenum Press: New York, 1998.
- (46) Banerjee, A. N.; Joo, S. W.; Kim, B. M. Photocatalytic Degradation of Organic Dye by Sol-Gel-Derived Gallium-Doped Anatase Titanium Oxide Nanoparticles for Environmental Remediation. *J. Nanomater.* **2012**, *2012*, No. 201492.
- (47) Guetta, N.; Ait-Amar, H. Photocatalytic oxidation of methyl orange in presence of titanium dioxide in aqueous suspension. Part II: Kinetics study. *Desalination* **2005**, *185*, 439–448.
- (48) Sheng, J. Y.; Li, X. J.; Xu, Y. M. Effect of Sintering Temperature on the Photocatalytic Activity of Flower-Like Bi₂WO₆. *Acta Phys. Chim. Sin.* **2014**, *30*, 508–512.
- (49) Barka, N.; Qourzal, S.; Assabbane, A.; Nounah, A.; Ait-Ichou, Y. Factors influencing the photocatalytic degradation of Rhodamine B by TiO₂-coated non-woven paper. *J. Photochem. Photobiol. A* **2008**, *195*, 346–351.
- (50) Stone, A. T. Reductive Dissolution of Manganese (III/IV) Oxides by Substituted Phenols. *Environ. Sci. Technol.* **1987**, *21*, 979–988.
- (51) Dang, T. D.; Banerjee, A. N.; Cheney, M. A.; Qian, S.; Joo, S. W.; Min, B. K. Bio-Silica Coated with Amorphous Manganese Oxide as an Efficient Catalyst for Rapid Degradation of Organic Pollutant. *Colloids Surf. B* **2013**, *106*, 151–157.
- (52) Wang, S.; Ma, W.; Jia, M.; Huang, Y. Degradation of Pollutants by Hydrophobic FePcCl₁₆ under Ultraviolet and Visible Light. *Fresenius Environ. Bull.* **2013**, *22*, 549–555.